Weak localization, spin relaxation, and spin diffusion: Crossover between weak and strong Rashba coupling limits

Yasufumi Araki, Guru Khalsa, and Allan H. MacDonald

Phys. Rev. B **90**, 125309 — Published 17 September 2014

DOI: 10.1103/PhysRevB.90.125309

Weak Localization, Spin Relaxation, and Spin-Diffusion: The Crossover Between Weak and Strong Rashba Coupling Limits

Yasufumi Araki,[1] Guru Khalsa,[1,2] and Allan H. MacDonald[1]

[1] *Department of Physics, University of Texas at Austin, Austin, Texas 78712, USA*
[2] *Center for Nanoscale Science and Technology, National Institute of Standards and Technology, Gaithersburg, MD 20899, USA*

Disorder scattering and spin-orbit coupling are together responsible for the diffusion and relaxation of spin-density in time-reversal invariant systems. We study spin-relaxation and diffusion in a two-dimensional electron gas with Rashba spin-orbit coupling and spin-independent disorder, focusing on the role of Rashba spin-orbit coupling in transport. Spin-orbit coupling contributes to spin relaxation, transforming the quantum interference contribution to conductivity from a negative weak localization (WL) correction to a positive weak anti-localization (WAL) correction. The importance of spin channel mixing in transport is largest in the regime where the Bloch state energy uncertainty $\hbar/\tau$ and the Rashba spin-orbit splitting $\Delta_{\rm SO}$ are comparable. We find that as a consequence of this spin channel mixing, the WL-WAL crossover is non-monotonic in this intermediate regime, which can be related to recent experimental studies of transport at two-dimensional oxide interfaces.

PACS numbers: 73.20.Fz,71.70.Ej,72.25.Rb,71.10.Ca

I. INTRODUCTION

Spin-orbit coupling, present whenever electrons move in a strong electric field, has recently been playing a more prominent role in electronics. When spin-orbit coupling is present, broken inversion symmetry lifts the two-fold spin-degeneracy of Bloch states in a crystal. For example, as pointed out by Rashba[1], spin-orbit coupling produces spin-splitting at surfaces and at interfaces between different materials. In spintronics, Rashba spin-orbit coupling can provide a handle for electrical control of spin since its strength and character depends not only on atomic structural asymmetry but also on external gate voltages[2], allowing for the possibility of a spin-based field-effect transistor.[3] Alternately, spin-splitting due to Rashba spin-orbit coupling in proximity coupled nanowires can lead to topological superconductivity and Majorana edge states[4], which can provide an attractive Hilbert space for quantum state manipulation for the purpose of quantum information processing.

Because spin-orbit coupling does not conserve spin, one of its most important consequences in spintronics is its role in providing a mechanism for relaxation of non-equilibrium spin densities. In the absence of spin-orbit coupling, total charge and all three components of total spin are conserved. Spin relaxation mechanisms due to spin-orbit coupling can be classified into two types: the Elliott–Yafet (EY) mechanism,[5,6] where skew-scattering due to spin-orbit interactions with scattering centers is the the most obvious spin-relaxation process, and the more subtle but equally important Dyakonov–Perel (DP) mechanism,[7] in which the momentum-dependent spin-orbit effective magnetic fields responsible for spin-splitting of the Bloch states cause spin-precession between collisions. The DP spin relaxation mechanism is often dominant in spintronics, and can cause subtle interplays between charge and spin transport.[8,9]

Spin relaxation has an important indirect effect on the quantum contribution to the conductivity. In weakly disordered metallic systems with no spin-orbit coupling, backscattering is enhanced by constructive interference between time-reversed paths (see Fig.1) yielding a negative quantum correction to the classical conductivity calculated from Drude's formula. This effect is referred to as weak localization (WL).[10–13] In two-dimensional systems, WL acts as a precursor to the transition into the Anderson insulator state in which disorder is sufficiently strong to localize electrons. When the spin degree-of-freedom is accounted for in the absence of spin-orbit coupling, spin-degeneracy multiplies the conductivity correction by a factor of two. In general there are four two-particle spin states which contribute to the interference. When parsed in terms of total spin eigenstates, interference between time-reversed paths is constructive for

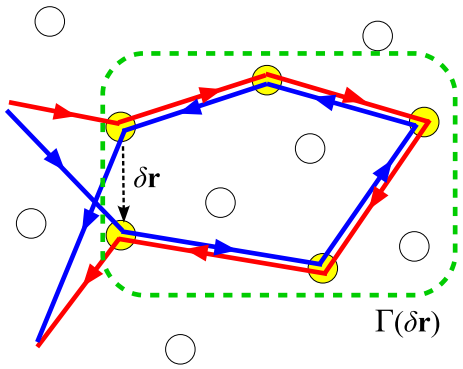

FIG. 1: (Color online) A schematic illustration of the the quantum correction to conductivity. Quantum interference between a closed electron path (red) and a nearly time-reversed counterpart (blue), alters the backscattering rate when $\mathbf{q}$, the sum of the two incoming momenta, is close to zero. The interference is constructive in the absence of spin-orbit coupling, enhancing back scattering and suppressing the diffusion constant and the conductivity, but can be destructive and enhance the conductivity when spin-orbit is present.

the three triplet channels, but destructive for the singlet channel because of the Berry phase contributed by rotation of the spin wave function along the path, recovering the factor of two enhancement. Spin relaxation changes this situation. Because the spin-density present in the triplet channels relaxes their contribution to the conductivity, the correction is reduced when spin-orbit coupling is present, whereas the singlet channel is unaffected due to charge conservation. When this effect is strong, either due to strong spin-orbit coupling or due to long phase coherence times, the quantum contribution becomes positive. In this case the quantum correction is referred to as weak antilocalization (WAL). WL and WAL can be identified by studying the temperature and magnetic field dependence of the conductivity, since these parameters limit the phase coherence length L, the characteristic length within which electrons can propagate without losing their phase coherence. The theory of WAL onset was developed microscopically by Hikami, Larkin and Nagaoka (HLN) using a model with EY spin-relaxation,[14] and later macroscopically using a nonlinear σ-model approach[15] which demonstrated that the effect depends mainly on global symmetries and not on microscopic details. Iordanskii, Lyanda-Geller and Pikus (ILP) later were the first to point out that DP spin relaxation also leads to WAL, and that the triplet channels contribution is modified compared to that implied by the EY mechanism.[16] WAL induced by DP spin relaxation has been identified as responsible for negative magnetoconductivity in quantum wells[17,18] and in topological insulator surface states.[19–21] A recent experiment on transport at the interface between $LaAlO_3$ (LAO) and $SrTiO_3$ (STO) has demonstrated that a WL-WAL crossover can be induced by gate voltage modulation.[22].

Motivated partly by the experiments in LAO/STO heterostructures, we attempt to investigate in detail the dependence of WL and WAL transport contributions on spin-orbit coupling strength across the crossover between resolved spin-splitting (where disorder broadening is much smaller than spin-orbit coupling) and spin-splitting obscured by disorder, by tuning the Rashba spin-orbit coupling strength in a two-dimensional electron gases (2DEG). This crossover is controlled by a competition between two energy scales: the Bloch state spin-splitting $\Delta_{\rm SO}$ induced by spin-orbit coupling in systems without inversion symmetry, and the Bloch state energy uncertainty η due to the finite lifetime of Bloch states in a disordered system. The asymptotic behavior in the extreme cases is obvious from the arguments we have summarized briefly above. In the band-unresolved limit ($\Delta_{\rm SO} \ll \eta$) we can apply ILP's analysis[16] by taking spin-orbit coupling into account perterbatively. In this limit WAL emerges from WL behavior in the long-phase coherence limit. On the other hand, in the band-resolved limit ($\Delta_{\rm SO} \gg \eta$), only the spin singlet channel contributes to quantum interference and we obtain perfect WAL behavior. What we intend to investigate here is the behavior in the intermediate regime ($\Delta_{\rm SO} \approx \eta$). For this purpose, we have developed tools which enable us to investigate spin-relaxation and diffusion, and to evaluate quantum corrections to Boltzmann transport at any value of $\Delta_{\rm SO}/\eta$. We have found that for a two-dimensional electron-gas model with Rashba spin-orbit interactions, spin relaxation in the intermediate regime cannot be simply described by ILP's picture. Spin relaxation is partially suppressed by interference between channels, leading to a new plateau on which the WL/WAL behavior is relatively insensitive to spin-orbit coupling strength. We suggest that such a behavior can be confirmed experimentally by tuning the spin-orbit coupling with gate voltage and fixing other parameters.

This paper is organized as follows. In Section II, we explain how we evaluate the low-energy long-wavelength limit of the electron-pair (Cooperon) propagator treating spin-orbit coupling and spin-relaxation it producees non-perturbatively. In Section III, we discuss our numerical results for the Cooperon of the Rashba model, and calculate the spin relaxation lengths for each triplet channel in order to characterize spin relaxation behavior across the crossover between the spin-resolved and unresolved limits. Using the spin-relaxation characteristics we have calculated, we summarize the WL-WAL crossover in Section IV, constructing a phase diagram in the $\Delta_{\rm SO}$-η plane which identifies three regimes: perfect WL, perfect WAL, and an intermediate plateau regime. Finally, in Section V, we briefly summarize our findings and present our conclusions.

II. MICROSCOPIC THEORY OF WL AND WAL

As a typical example of a system with broken inversion symmetry, we consider an isotropic 2DEG band Hamiltonian with a Rashba spin-orbit interaction term,

$$\hat{H}(\mathbf{k}) = \mathbf{k}^2 + \hat{\sigma}_i h_i(\mathbf{k}), \tag{1}$$

where we have set $\hbar = 1$ so that wave vector can be identified as momentum and for simplicity rescaled momentum to set $2m = 1$. We distinguish 2×2 matrices in the spin-up/down representation by a *hat* accent. The second term in Eq. 1 allows for arbitrary spin-orbit coupling given a model with a single spin-split band. ($\hat{\sigma}_i$ $(i = x, y, z)$ are Pauli matrices.) For the Rashba model, the effective magnetic field is perpendicular to momentum $\mathbf{k}$. and has a coupling strength characterized by the parameter α: $\mathbf{h}(\mathbf{k}) = \alpha(k_y, -k_x, 0)$. Rashba coupling is symmetry-allowed in systems in which inversion symmetry is broken because the two-dimensional system is not a mirror plane. For example Rashba coupling can be induced by a gate-induced electric-field perpendicular to the two-dimensional electron gas plane. It leads to spin-splitting $2\alpha k$ at momentum k, where the band energies are

$$E_n(\mathbf{k}) = k^2 + n\alpha k, \tag{2}$$

with band index $n = \pm 1$. Limiting the Fermi energy ϵ_F to be positive, the two bands have Fermi surfaces with different Fermi radii $k_{Fn} = (v_F - n\alpha)/2$, but equal Fermi velocities $v_F = \sqrt{\alpha^2 + 4\epsilon_F}$. In this article we define $\Delta_{\rm SO} = 2\alpha\bar{k}_F$ and use this number to characterize the strength of spin-orbit coupling at the Fermi energy. Here $\bar{k}_F = (k_{F+} + k_{F-})/2 = v_F/2$ is the typical value of the Fermi momentum, independent of n.

We assume a disorder model with randomly-distributed, spin-independent, δ-function scatterers:

$$\hat{H}_{\rm dis}(\mathbf{r}) = V \sum_{i=1}^{N} \delta(\mathbf{r} - \mathbf{r}_i), \tag{3}$$

where N is the total number of impurities. After disorder averaging disorder vertices are linked in pairs with four-point vertex amplitude $NV^2/\Omega^2 \equiv \gamma/\Omega$, where Ω is the volume of the system. Thus, the disorder unaveraged one-particle Green's function $\hat{G}_0^{\pm} = \left[\epsilon_F - \hat{H} - \hat{H}_{\rm dis} \pm i0\right]^{-1}$ reduces to a translationally invariant one,

$$\hat{G}^{\pm}(\mathbf{k}) = \left\langle \hat{G}_0^{\pm}(\mathbf{k},\mathbf{k}) \right\rangle_{\rm dis} = \frac{1}{\epsilon_F - \hat{H}(\mathbf{k}) \pm i\eta}, \tag{4}$$

in the Born approximation, where $\pm$ distinguishes retarded and advanced Green's functions, $\langle\cdot\rangle_{\rm dis}$ represents the average over disorder configuration, and

$$\eta = \frac{1}{2\tau} = -\frac{\gamma}{\Omega}{\rm Im}\sum_{\mathbf{k}} G^{+}(\mathbf{k}) = \frac{\gamma}{4}. \tag{5}$$

The spectral weight of the Green's function is spread over the energy interval η, corresponding to the finite-lifetime energy uncertainty of the Bloch states. When $\Delta_{\rm SO} \ll \eta$, the two bands are degenerate to within energy resolution and the role of spin-orbit interactions is simply to cause spin-precession between collisions. When $\Delta_{\rm SO} \gg \eta$, on the other hand, the two-band energies are well resolved and coherence between bands is negligible. In our analysis we assume that $\Delta_{\rm SO}, \eta \ll \epsilon_F$, the normal experimental situation, but allow the ratio $\Delta_{\rm SO}/\eta$ to vary. In our discussion section, we comment briefly on the $\Delta_{\rm SO}, \eta \gg \epsilon_F$ case, which corresponds closely to the circumstance achieved in topological insulator surface states.

In general, the longitudinal conductivity at zero temperature is given by the Kubo–Streda formula,

$$\sigma = \frac{1}{2\pi\Omega}{\rm Re}\sum_{\mathbf{k},\mathbf{k}'} {\rm Tr}\left\langle \hat{j}_x(\mathbf{k})\hat{G}_0^{+}(\mathbf{k},\mathbf{k}')\hat{j}_x(\mathbf{k}')\hat{G}_0^{-}(\mathbf{k}',\mathbf{k})\right\rangle_{\rm dis}, \tag{6}$$

where the current matrix is defined by $\hat{j}_x(\mathbf{k}) = e\hat{v}_x(\mathbf{k}) = e[\partial\hat{H}(\mathbf{k})/\partial k_x]$. For δ-function scatterers the semiclassical Boltzmann theory result for the conductivity, namely Drude's formula, is recovered by disorder-averaging the two Green's functions separately:

$$\sigma_0 = \frac{1}{2\pi\Omega}{\rm Re}\sum_{\mathbf{k}} {\rm Tr}\left[\hat{j}_x(\mathbf{k})\hat{G}^{+}(\mathbf{k})\hat{j}_x(\mathbf{k})\hat{G}^{-}(\mathbf{k})\right]. \tag{7}$$

σ_0 is proportional to the density of states at the Fermi energy. Since the total density of states at fixed ϵ_F is independent of α, the classical conductivity σ_0 is independent of α provided that $\Delta_{\rm SO}$ is small compared to the Fermi energy ϵ_F.

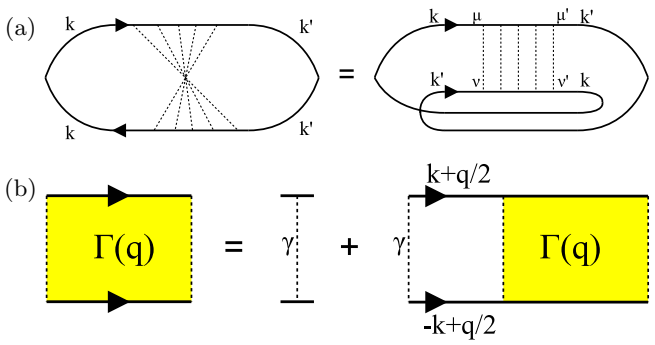

FIG. 2: (Color online) Feynman diagrams for the dominant quantum correction to the conductivity. (a) The upper line and lower lines represent the retarded and advanced Green's functions $\hat{G}^{\pm}$, respectively. The maximally crossed diagrams can be reorganized into a particle-particle ladder-diagram sum. (b) Graphical representation of the ladder diagram sum for the Cooperon which can be performed by solving a Bethe–Salpeter equation.

The leading quantum correction to the conductivity comes from the interference between a closed multiple-scattering path and its time-reversed counterpart, as illustrated in Fig.1. In its diagrammatic representation, the sum of this interference over all classical paths is captured by summing the diagrams in which disorder interaction lines connecting the retarded and advanced Green's functions are maximally crossed, as illustrated in Fig. 2(a). The particle-particle ladder diagram sum is referred to as the Cooperon $\check{\Gamma}(\mathbf{q})$, with $\mathbf{q} = \mathbf{k} + \mathbf{k}'$ the total momentum flowing into the Cooperon, or equivalently the deviation from the perfect backscattering which occurs for $\mathbf{q} = 0$. In the following we distinguish matrices in the 4×4 tensor product space, with the basis $\{|\uparrow\uparrow\rangle, |\uparrow\downarrow\rangle, |\downarrow\uparrow\rangle, |\downarrow\downarrow\rangle\}$, by a *check* accent over the letters as in $\check{O}$. The contribution of the Cooperon to the conductivity is

$$\begin{aligned}\Delta\sigma &= \frac{\rm Re}{2\pi\Omega}\sum_{\mathbf{k},\mathbf{k}'}(\hat{G}^{-}\hat{j}_x\hat{G}^{+})_{\nu'\mu}(\mathbf{k})\check{\Gamma}^{\mu\mu'}_{\nu\nu'}(\mathbf{q})(\hat{G}^{+}\hat{j}_x\hat{G}^{-})_{\mu'\nu}(\mathbf{k}') \\ &= \frac{e^2}{2\pi}{\rm ReTr}\left[\check{W}\sum_{\mathbf{q}}\check{\Gamma}(\mathbf{q})\right],\end{aligned} \tag{8}$$

where μ, μ', ν, ν' take the spin indices $\uparrow$ or $\downarrow$. We will assume that $\check{\Gamma}(\mathbf{q})$ has a peak at backscattering $\mathbf{q} = 0$, and

that it is large only for small total momentum $\mathbf{q}=\mathbf{k}+\mathbf{k}'$. The area of summation by $\mathbf{q}$ is limited by the characteristic length scales of the system. The lower cutoff is given by the inverse of a large length scale L, within which the electron can move without losing its phase coherence. L acts like the (effective) size of a phase coherent system. The length scale L decreases with increasing temperature due to increased inelastic scattering by phonons or other electrons, or with an increase of magnetic field due to the cyclotron motion of the Cooper pair center of mass. In our analysis, we represent both effects by the length L. The upper wave vector cutoff is given by the inverse of the elastic mean free path $l=\sqrt{2D\tau}$, above which electron dynamics is ballistic rather than diffusive. Here $D=v_F^2\tau/2$ is the diffusion coefficient.

The *weight factor* ($\check{W}$) in Eq. 8 specifies how each Cooperon channel contributes to the conductivity, and is defined by

$$\check{W}^{\mu'\mu}_{\nu'\nu}=\frac{1}{\Omega}\sum_{\mathbf{k}}(\hat{G}^-\hat{v}_x\hat{G}^+)_{\nu'\mu}(\mathbf{k})(\hat{G}^+\hat{v}_x\hat{G}^-)_{\mu'\nu}(-\mathbf{k}). \quad (9)$$

Since the original Hamiltonian is isotropic, the matrix structure of $\check{W}$ is not changed by coordinate rotations which replace $\hat{v}_x$ by velocity in some other direction.

The Cooperon factor ($\check{\Gamma}(\mathbf{q})$) in Eq. 8 is defined as an infinite sum of ladder diagrams,

$$\check{\Gamma}(\mathbf{q})=\frac{\gamma}{\Omega}+\frac{\gamma}{\Omega}\Omega\check{P}(\mathbf{q})\frac{\gamma}{\Omega}+\frac{\gamma}{\Omega}\Omega\check{P}(\mathbf{q})\frac{\gamma}{\Omega}\Omega\check{P}(\mathbf{q})\frac{\gamma}{\Omega}+\cdots. \quad (10)$$

The structure factor $\check{P}$ associated with a single rung of the ladder, is given by the tensor product

$$\check{P}(\mathbf{q})=\frac{1}{\Omega}\sum_{\mathbf{k}}\hat{G}^+(\mathbf{k}+\tfrac{\mathbf{q}}{2})\otimes\hat{G}^-(-\mathbf{k}+\tfrac{\mathbf{q}}{2}). \quad (11)$$

Eq.(10) can be summed analytically by solving an algebraic equation as illustrated in Fig. 2(b), to obtain

$$\check{\Gamma}(\mathbf{q})=\frac{1}{\Omega}\left[\gamma^{-1}-\check{P}(\mathbf{q})\right]^{-1}. \quad (12)$$

Thus the matrix structure of $\check{P}(\mathbf{q})$ determines which Cooperon channel contribute to the conductivity correction. Eigenvalues of $\check{P}(\mathbf{q})$ that are close to γ^{-1} lead to large contributions to the conductivity. In the next section, we investigate the matrix structure of Cooperon in detail, and calculate the conductivity correction as a function of the Rashba coupling constant α both analytically and numerically.

III. EVALUATION OF THE CHARACTERISTIC FACTORS

A. Cooperon

Since we expect the Cooperon to be large only in the vicinity of backscattering, we set $\mathbf{q}=q(\cos\theta,\sin\theta)$ and expand $\check{P}(\mathbf{q})$ in powers of q up to order $O(q^2)$:

$$\check{P}(\mathbf{q})=\check{P}^{(0)}+q\check{P}^{(1)}_\theta+q^2\check{P}^{(2)}_\theta+O(q^3). \quad (13)$$

We obtain the following expressions for the expansion coefficients:

$$\check{P}^{(0)}=\frac{1}{\Omega}\sum_{\mathbf{k}}\hat{G}^+\otimes\underline{\hat{G}}^- \quad (14)$$

$$\check{P}^{(1)}_\theta=\frac{1}{2\Omega}\sum_{\mathbf{k}}\left[(\hat{G}^+\hat{v}_\theta\hat{G}^+)\otimes\underline{\hat{G}}^-+\hat{G}^+\otimes(\underline{\hat{G}}^-\underline{\hat{v}}_\theta\underline{\hat{G}}^-)\right]$$

$$\check{P}^{(2)}_\theta=\frac{1}{2\Omega}\sum_{\mathbf{k}}\left[(\hat{G}^+\hat{v}_\theta\hat{G}^+)\otimes(\underline{\hat{G}}^-\underline{\hat{v}}_\theta\underline{\hat{G}}^-)\right],$$

where the underlined matrices are evaluated at momentum $-\mathbf{k}$, and other matrices are evaluated at $\mathbf{k}$. $\hat{v}_\theta$ denotes the velocity projected onto the direction of $\mathbf{q}$: $\hat{v}_\theta=\hat{v}_x\cos\theta+\hat{v}_y\sin\theta$. In the spinless (or $\alpha=0$) case the expansion simplifies to $P(q)=\gamma^{-1}[1-D\tau q^2]$. The Cooperon therefore has a pole at $q=0$ and this leads to the well-known WL correction to the conductivity. Our goal here is to investigate the deviation from conventional Cooperon structure due to Rashba spin-orbit coupling.

The matrix structure of $\check{P}(\mathbf{q})$ can be understood through the symmetries of the Hamiltonian. Consider a spin rotation by π around the in-plane axis perpendicular to the $\mathbf{q}$-direction generated by the Pauli matrix

$$\hat{\sigma}_\theta\equiv\hat{\sigma}_y\cos\theta-\hat{\sigma}_x\sin\theta=\begin{pmatrix}0 & e^{-i(\theta-\pi/2)}\\ e^{i(\theta-\pi/2)} & 0\end{pmatrix}. \quad (15)$$

The unitary transformation $\hat{\sigma}_\theta$ transforms the Rashba Hamiltonian $\hat{\sigma}_i h_i(\mathbf{k})$ to $\hat{\sigma}_i h_i(\mathbf{k}')$, where $\mathbf{k}'$ is the mirror reflection of $\mathbf{k}$ in a plane perpendicular to $\mathbf{q}$. Thus, the Green's function $\hat{G}^\pm(\pm\mathbf{k}+\frac{\mathbf{q}}{2})$ gets rotated to $\hat{G}^\pm(\pm\mathbf{k}'+\frac{\mathbf{q}}{2})$. By replacing the summation over $\mathbf{k}$ by one over $\mathbf{k}'$ we can conclude that $\check{P}(\mathbf{q})$ in Eq. (11) is invariant under $\check{\Sigma}_\theta\equiv\hat{\sigma}_\theta\otimes\hat{\sigma}_\theta$. It follows that $\check{P}(\mathbf{q})$ and $\check{\Sigma}_\theta$ can be diagonalized simultaneously. Since the eigenstates of $\check{\Sigma}_\theta$ are twofold degenerate, with the eigenvalues ±1 respectively, $\check{P}(\mathbf{q})$ is at least block diagonal in this basis.

Next consider spin rotation by π around the z-axis which is generated by $\hat{\sigma}_z$. Since this operation transforms the Rashba term $\hat{\sigma}_i h_i(\mathbf{k})$ to $\hat{\sigma}_i h_i(-\mathbf{k})$, $\check{P}(\mathbf{q})$ goes to $\check{P}(-\mathbf{q})$ under the unitary transformation $\check{\Sigma}_z\equiv\hat{\sigma}_z\otimes\hat{\sigma}_z$. Although $\check{P}(\mathbf{q})$ is not invariant under this transformation, even-ordered expansion terms like $\check{P}^{(0)}$ and $\check{P}^{(2)}$ are invariant. It follows that these terms are diagonal in the representation formed by the mutual eigenstates of $\check{\Sigma}_\theta$ and $\check{\Sigma}_z$:

$$\begin{pmatrix}|\chi_1\rangle\\ |\chi_2\rangle\\ |\chi_3\rangle\\ |\chi_4\rangle\end{pmatrix}=\frac{1}{\sqrt{2}}\begin{pmatrix}e^{i\theta} & & & -e^{-i\theta}\\ & 1 & 1 & \\ & 1 & -1 & \\ e^{i\theta} & & & e^{-i\theta}\end{pmatrix}\begin{pmatrix}|\uparrow\uparrow\rangle\\ |\uparrow\downarrow\rangle\\ |\downarrow\uparrow\rangle\\ |\downarrow\downarrow\rangle\end{pmatrix}. \quad (16)$$

This argument does not rule out off-diagonal elements in each block of $\check{P}^{(1)}$. In fact as we emphasize later these

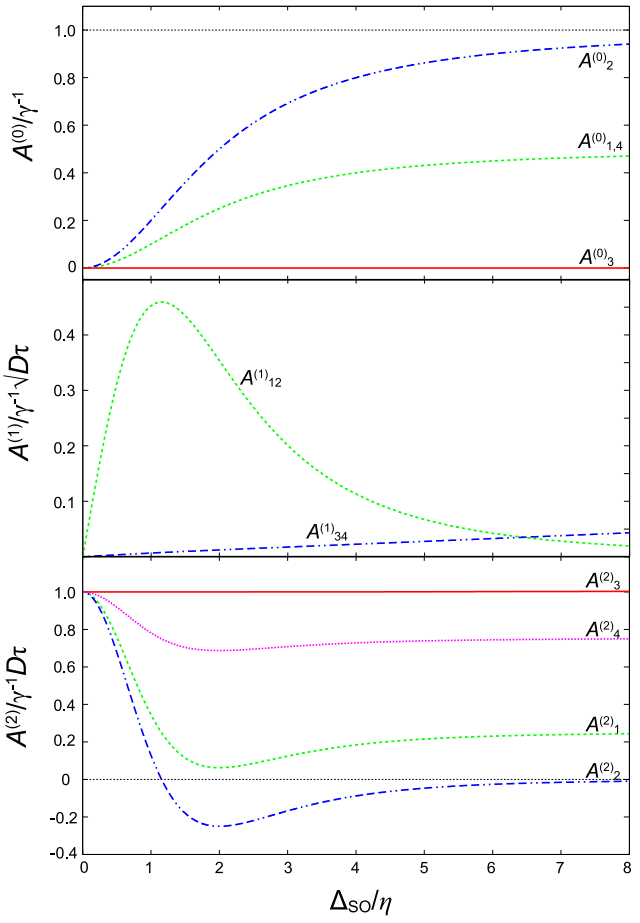

FIG. 3: (Color online) Matrix elements of $\check{\Gamma}^{-1}(\mathbf{q}) = \gamma^{-1} - \check{P}(\mathbf{q})$ at zeroth, first, and second order in a wave vector magnitude (q) expansion. The illustrated calculation was for $\eta/\epsilon_F = 0.01$. The horizontal axis is the Rashba band splitting $\Delta_{SO} = 2\alpha k_F$ normalized by η. The plotted quantities are defined in Eq.(18).

terms do appear in $\check{P}^{(1)}$ and are responsible for anomalous spin relaxation behavior. We will refer to this representation as the "singlet-triplet basis", since $|\chi_3\rangle$ corresponds to the spin singlet state. and the other three states span the three triplet states. Note that this two-particle basis depends on the direction of $\mathbf{q}$.

We now discuss the numerical evaluation of the $\check{P}(\mathbf{q})$ wave-vector-magnitude expansion coefficients defined in Eqs. (14) as a function of the Rashba coupling strength α. We make all physical quantities dimensionless by invoking scale transformations which reduce the Fermi energy ϵ_F and the mass $2m$ to unity. As explained in more detail in Appendix A, the momentum integrations can be performed analytically by using a gradient expansion around the Fermi level and extending the integration contour to a closed path in the complex plane. We calculate the structure factor matrix $\check{P}(\mathbf{q})$ in the singlet-triplet basis motivated above. The Cooperon, $\check{\Gamma}(\mathbf{q}) = \Omega^{-1}\left[\gamma^{-1} - \check{P}(\mathbf{q})\right]^{-1}$, has the block-diagonal matrix structure

$$\check{\Gamma}(\mathbf{q}) = \frac{1}{\Omega}\begin{pmatrix} \hat{\Gamma}_{12}(q) & 0 \\ 0 & \hat{\Gamma}_{34}(q) \end{pmatrix}, \tag{17}$$

with

$$\hat{\Gamma}^{-1}_{12}(q) = \begin{pmatrix} A^{(0)}_1 + q^2 A^{(2)}_1 & iqA^{(1)}_{12} \\ -iqA^{(1)}_{12} & A^{(0)}_2 + q^2 A^{(2)}_2 \end{pmatrix} \tag{18}$$

$$\hat{\Gamma}^{-1}_{34}(q) = \begin{pmatrix} q^2 A^{(2)}_3 & qA^{(1)}_{34} \\ -qA^{(1)}_{34} & A^{(0)}_4 + q^2 A^{(2)}_4 \end{pmatrix}.$$

The definitions of the coefficients $A^{(0)}$, $A^{(1)}$ and $A^{(2)}$ are given in Appendix A. In Fig.3 all distinct expansion coefficients are plotted as a function of the Rashba coupling strength α. (Since $A^{(1)}$ is zero for $\alpha = 0$, we normalize it by $\gamma^{-1}\sqrt{D\tau}$, which is comparable to $\sqrt{A^{(0)}A^{(2)}}$.)

For orientation we first comment on the characteristic behavior of these coefficients under some extreme conditions:

- When the spin-orbit coupling is switched off ($\alpha = 0$), all the constant $A^{(0)}$ and linear $A^{(1)}$ coefficients vanish, and the quadratic coefficients $A^{(2)}$ reduce to $D\tau/\gamma$. This result for the Cooperon leads to the conventional WL expression for the maximally-crossed diagram correction to the conductivity of a 2DEG that is free of spin-orbit coupling.

- When $\Delta_{SO} \ll \eta$, $A^{(0)}$ and $A^{(2)}$ depart from their degenerate values by $O(\alpha^2)$, while $A^{(1)}$ is $O(\alpha^1)$. These findings agree with results obtained by ILP[16] by treating Rashba spin-orbit coupling as a perturbation.

- In the strong ($\Delta_{SO} \gg \eta$) spin-orbit coupling limit, $A^{(0)}$ and $A^{(2)}$ reach asymptotic values with the ratios

$$A^{(0)}_1 : A^{(0)}_2 : A^{(0)}_3 : A^{(0)}_4 = 1:2:0:1 \tag{19}$$
$$A^{(2)}_1 : A^{(2)}_2 : A^{(2)}_3 : A^{(2)}_4 = 1:0:4:3,$$

  which coincides with the behavior of the Cooperon coefficients of the massless Dirac Hamiltonian. The Rashba and massless Dirac models agree in this limit because the eigenstates of the two models have the same structure. The agreement occurs even though the Rashba model normally has two Fermi surfaces, whereas the massless Dirac model always has a single Fermi surface.

Fig.3 describes the crossover behavior of the Cooperon from the weak spin-orbit coupling regime captured by ILP's analysis,[16] to the strongly spin-orbit coupled limit with partial equivalence between massless Dirac and Rashba models. Since the spin singlet channel is unaffected by the Rashba internal magnetic field $\mathbf{h}(\mathbf{k})$, the coefficients $A^{(0)}_3$ and $A^{(2)}_3$ for the singlet channel are independent of α.

It is important here to note the behavior of the $O(q^1)$ term, which is absent in the spinless model. Its off-diagonal components give rise to mixing between different spin channels. Although the mixing between the singlet channel and one of the triplet channels, specified by $A_{34}^{(1)}$, is weak provided only that $\Delta_{\rm SO} \ll \epsilon_F$, the mixing between two triplet channels, specified by $A_{12}^{(1)}$ shows quite a nontrivial behavior. It vanishes in both strong and weak spin-orbit coupling limits: $A_{12}^{(1)} \propto \epsilon_F^{1/2}\Delta_{\rm SO}/8\eta^3$ in the band unresolved limit, and $A_{12}^{(1)} \propto 2\epsilon_F^{1/2}\eta/\Delta_{\rm SO}^3$ in the resolved spin-splitting limit. In the intermediate regime ($\Delta_{\rm SO} \approx \eta$), on the other hand, it is $\sim O(\sqrt{A^{(0)}A^{(2)}})$. The Cooperon behavior shown here is the time-reversal counterpart of the spin diffusion under the Rashba spin splitting[9]. Spin relaxation is no longer described by simple exponential decay, but rather like a damped oscillation in which spins precess as they relax. We elaborate on this point in the next subsection.

B. Spin relaxation

Using the symmetry-dictated block-diagonal structure of the $\check{P}(q)$ matrix in the singlet-triplet basis, we can express the Cooperon in terms of its non-zero matrix elements,

$$\check{\Gamma}(\mathbf{q}) = \frac{1}{\Omega}\begin{pmatrix} X_{11} & X_{12} & 0 & 0 \\ X_{21} & X_{22} & 0 & 0 \\ 0 & 0 & X_{33} & X_{34} \\ 0 & 0 & X_{43} & X_{44}. \end{pmatrix}, \qquad (20)$$

The elements $X_{ij}(q)$ are determined by inverting Eqs.(18). Since the singlet-triplet basis depends on the direction of the momentum $\mathbf{q}$, we need to change the basis back to a momentum independent form before taking the sum over $\mathbf{q}$ in Eq. (8). Going back to the tensor product basis and integrating out the angular dependence we obtain

$$\sum_{\mathbf{q}} \check{\Gamma}(\mathbf{q}) = \int_{L^{-1}}^{l^{-1}} \frac{dq\ q}{2\pi} \begin{pmatrix} \tilde{X}_1(q) & & & \\ & \tilde{X}_2(q) & \tilde{X}_3(q) & \\ & \tilde{X}_3(q) & \tilde{X}_2(q) & \\ & & & \tilde{X}_1(q) \end{pmatrix}, \qquad (21)$$

where

$$\tilde{X}_1 = \frac{X_{11}+X_{44}}{2},\ \tilde{X}_2 = \frac{X_{22}+X_{33}}{2}, \tilde{X}_3 = \frac{X_{22}-X_{33}}{2}. \qquad (22)$$

Thus we need to calculate only the diagonal elements of the Cooperon matrix in Eq.(20). When there is no linear term in q, as in the spin-orbit decoupled limit, each diagonal element has a diffusion peak; for example $X_{11} = [A_1^{(0)} + q^2 A_1^{(2)}]^{-1}$. The $O(q)$ terms in the inverse matrix mix contributions from the two channels in each block.

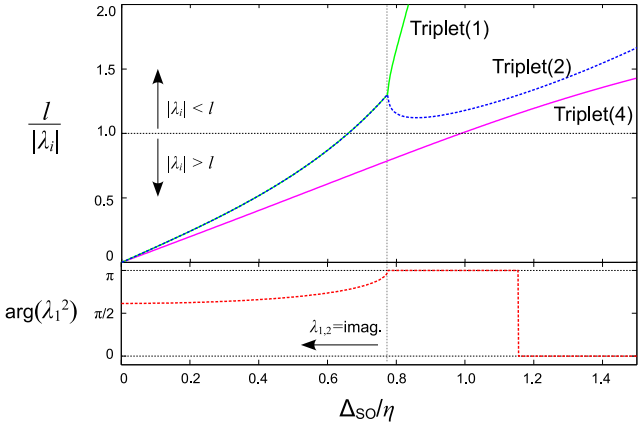

FIG. 4: (Color online) Upper panel: Inverse relaxation length $|\lambda_i|$ for each channel, normalized by the mean free path l. The triplet channels 1,2 and 4 belong to the eigenstates of $\Gamma(q)$ in Eq. (17), which are linear combinations of the triplet basis in Eq.(16). Lower panel: The argument of λ_1^{-2} normalized by π. The values plotted in this figure were calculated for $\eta/\epsilon_F = 0.01$. It should be noted that $\lambda_{1,2}$ is complex for $\Delta_{\rm SO} \lesssim 0.8\eta$, where the $O(q^1)$ channel mixing effect is dominant.

The diagonal elements are then conveniently expressed in terms of partial fraction decompositions with the form:

$$X_{11} = \frac{c_{11}}{\lambda_1^{-2}+q^2} + \frac{c_{12}}{\lambda_2^{-2}+q^2},\ X_{22} = \frac{c_{21}}{\lambda_1^{-2}+q^2} + \frac{c_{22}}{\lambda_2^{-2}+q^2},$$
$$X_{33} = \frac{c_{33}}{q^2} + \frac{c_{34}}{\lambda_4^{-2}+q^2},\quad X_{44} = \frac{c_{44}}{\lambda_4^{-2}+q^2}. \qquad (23)$$

The wavelengths λ in the denominators, whose dependence on spin-orbit coupling strength is plotted in Fig. 4, determine the characteristic length scales within which particle-hole pairs in different channels can propagate without loss. $\lambda_{1,2,4}$ are the "relaxation lengths" for triplet channels, which correspond to $\mathbf{q}$-dependent linear combinations of $|\chi_1\rangle, |\chi_2\rangle$ and $|\chi_4\rangle$. Recall that λ is infinite in the spinless case, i.e. $\lambda_3^{-2} = 0$.

The maximally crossed diagram contribution to the conductivity is proportional to an integral over wave vector magnitude of the diagonal elements of the Cooperon matrix. When corrections to the conductivity are substantial this integral is dominated by contributions from small q where our wave vector expansion is valid. These considerations lead to a sum over channels of the familiar logarithmic integral:

$$\int_{L^{-1}}^{l^{-1}} \frac{dq\ q}{2\pi} \frac{c}{\lambda^{-2}+q^2} = \frac{c}{4\pi} \ln \frac{1+(\lambda/l)^2}{1+(\lambda/L)^2}. \qquad (24)$$

The quantum correction to the conductivity is determined by three length scales: the mean free path l, the phase length L, which has simple power law dependences on temperature and magnetic field, and the spin relaxation length λ. We note that

- (i) When the spin relaxation length λ is long compared to L, *i.e.* for $l < L \ll \lambda$, the quantum inter-

ference is proportional to $\ln(L/l)$, leading to its familiar simple logarithmic temperature dependence.

- (ii) In the intermediate regime $l < \lambda < L$, the quantum interference correction from a particular channel is logarithmically dependent on its spin relaxation length λ, *i.e.* it is proportional to $\ln(\lambda/l)$.

- (iii) When λ is comparable to or even shorter than the mean free path l, *i.e.* for $\lambda \lesssim l$, the quantum interference correction is absent. Eq.(24) approaches zero for $\lambda^{-1} \to \infty$.

As we increase the spin-orbit coupling strength α, the relaxation length for the spin singlet channel λ_3 remains infinite (i.e. $\lambda_3^{-2} = 0$), which implies that the logarithmic contribution from X_{33} is unchanged by spin-orbit coupling. The behavior of λ_i for the other channels is illustrated in Fig.4. Since $\lambda_{1,2,4}$ are comparable to the mean free path when $\Delta_{\rm SO}$ is sufficiently large compared to η, we can see that only the spin singlet channel contributes to the quantum interference in this region. Since we are interested in the crossover between WL and WAL behavior, the region of α (or $\Delta_{\rm SO}$) that we need to investigate lies below this value.

We should note that $\lambda_{1,2}$ can take imaginary values at small α, because of the strong mixing between channels proportional to $qA_{12}^{(1)}$. Up to the first order in α, $\lambda_{1,2}^{-1} = \alpha\sqrt{(-1 \pm \sqrt{7}i)/2}$. In the context of spin diffusion, this imaginary spin relaxation implies damped oscillations in the spin density distribution[8]. In our calculation, especially in case (ii) in the above classification, it leads to a deviation from the simple logarithmic behavior $\sim \ln|\lambda/l|$, which comes from the argument angle of λ^{-1}. An imaginary λ suppresses the spin channel contributions to the quantum transport corrections to some extent compared to the case of real λ.

C. Weight factor

The quantum transport correction contributed by each channel is also influenced by the weight factor factor matrix $\check{W}$, defined in Eq. (9). Its evaluation is closely analogous to that required for the $O(q^2)$ term of the Cooperon. The matrix structure in the tensor product basis is,

$$\check{W} = \begin{pmatrix} -R_2 & & & -R_1 \\ & R_1+R_3 & -R_2' & \\ & -R_2' & R_1+R_3 & \\ -R_1 & & & -R_2 \end{pmatrix}. \qquad (25)$$

Detailed expressions for R_1, R_2, R_2' and R_3 are provided in Appendix A.

So far we have explained the matrix structure of the Cooperon and the weight factor. Using Eqs.(21) and (25)

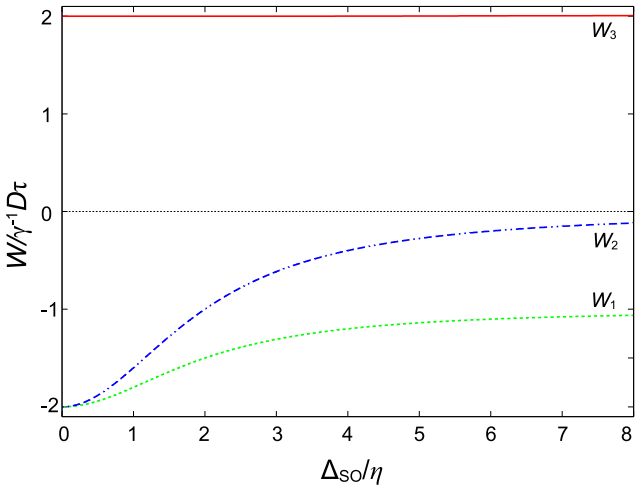

FIG. 5: (Color online) Behavior of the weight factors $W_{1,2,3}$ as a function of $\Delta_{\rm SO}/\eta$. The results illustrated here were calculated at $\eta/\epsilon_F = 0.01$.

we find that

$$\Delta\sigma = \frac{e^2}{2\pi}\int_{L^{-1}}^{l^{-1}} \frac{dq\ q}{2\pi}\left[W_1(X_{11}+X_{44}) + W_2X_{22} + W_3X_{33}\right], \qquad (26)$$

where the scalar weight factors

$$W_1 = -R_2,\ W_2 = R_1 + R_3 - R_2',\ W_3 = R_1 + R_3 + R_2', \qquad (27)$$

are plotted in Fig.5. When there is no spin-orbit coupling, all the weight factors have the same absolute values, $W_1 = W_2 = -W_3 = W_0$, where $W_0 = -2D\tau/\gamma$ is the WL weight factor in the spinless case. The minus sign in W_3, which is the weight factor for the spin-singlet channel, comes from the Berry phase due to spin rotation along the closed path. The weight for the singlet channel, W_3, is essentially constant for $\alpha \neq 0$ and gives rise to WAL, while the other weight factors which contribute to WL are suppressed. Since the contribution from the WL channels vanishes at large spin-orbit coupling due to the spin relaxation, only the WAL channel contributes to the quantum correction, in agreement with conventional arguments concluding that the EY mechanism gives rise to WAL.[14]

IV. TOTAL CORRECTION TO THE CONDUCTIVITY

Finally we use Eq.(26) to calculate the conductivity correction $\Delta\sigma$ as a function of the disorder amplitude η, the spin-orbit coupling strength α, and the phase coherence length L (determined by temperature, magnetic field, etc.). In the spinless case, we have the conventional logarithmic WL behavior, $\Delta\sigma_0(L) = -(e^2/2\pi)\ln(L/l)$.

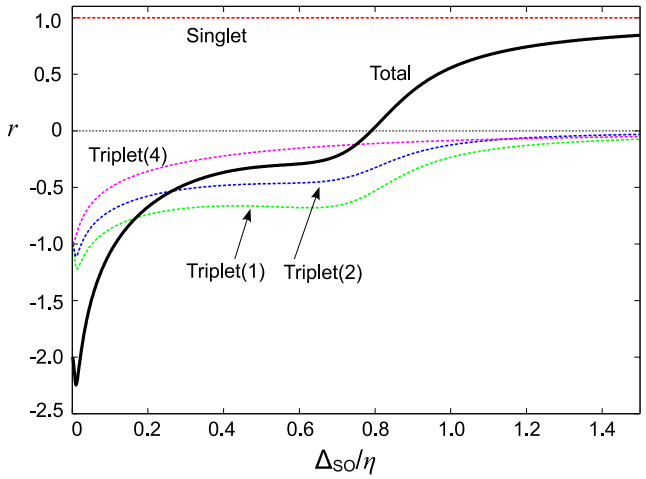

FIG. 6: (Color online) The quantum correction ratio $r(\alpha, L)$ as a function of the band splitting $\Delta_{\rm SO} = 2\alpha\bar{k}_F$, where the scattering amplitude and the phase coherence length are fixed at $\eta/\epsilon_F = 0.01$ and $L/l = 100$, respectively. The dashed lines show the contributions from the singlet and the three triplet channels X_{ii}, while the black bold line shows the total contribution. The triplet channels 1,2 and 4 belong to the eigenstates of $\Gamma(q)$ in Eq. (17), which are linear combinations of the triplet basis in Eq.(16). Note that the WL initially strengthens, then weakens and changes to WAL. There is a plateau in the Δ_{SO} dependence of r at intermediate values.

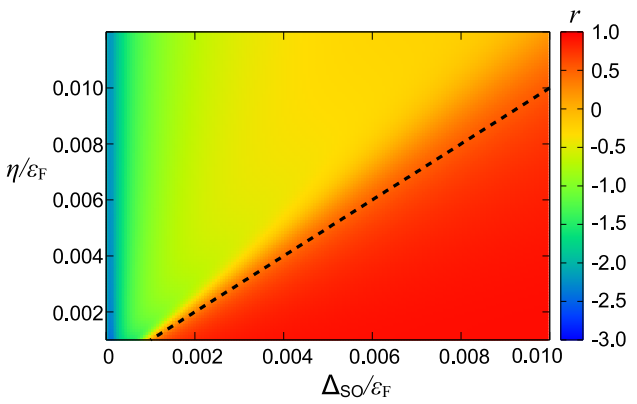

FIG. 7: (Color online) The quantum correction ratio $r(\alpha, L)$ *vs.* the band splitting $\Delta_{\rm SO} = 2\alpha\bar{k}_F$ and the scattering lifetime energy-uncertainty η. The phase coherence length is fixed at $L = 2 \times 10^4$, which is about 10-100 times larger than the mean free path l (depending on η). The black dashed line is $\Delta_{\rm SO} = \eta$. Note that weak-localization is initially enhanced ($r < -2$) by very weak spin-orbit coupling.

In our calculation we calculate the ratio r of the quantum correction amplitude to that of the spinless model:

$$r(\alpha, L) = \frac{\Delta\sigma(\alpha, L)}{|\Delta\sigma_0(L)|}. \tag{28}$$

When there is no spin-orbit coupling, $r = -2$, *i.e.* two degenerate modes contribute to WL. When the band splitting $\Delta_{\rm SO}$ is large enough, $r = 1$, i.e. only the spin singlet mode contributes and it leads to WAL. Here we calculate the detailed behavior of the ratio $r(\alpha, L)$ as $\Delta_{\rm SO}/\eta$ is varied to crossover between these two extreme limits.

First, we fix the scattering amplitude η and the coherence length L, and vary the Rashba coupling strength α, to investigate the crossover behavior going from full WL ($\alpha \sim 0$; $r = -2$) to the full WAL ($\Delta_{\rm SO} \gg \eta$; $r = 1$). This type of behavior is similar to that which might be expected experimentally when gates are used to vary the Rashba coupling strength at fixed temperature. In Fig.6 the ratio $r(\alpha, L)$ is plotted as a function of α, with the other parameters fixed at $\eta/\epsilon_F = 0.01$ and $L/l = 100$. We can see from this figure that an unexpected plateau-like structure appears in the intermediate region below $\Delta_{\rm SO} \approx \eta$, in addition to the expected *perfect WAL* plateau at $\Delta_{\rm SO} \gg \eta$. Interestingly this double-plateau structure cannot be described in the simple spin relaxation picture, obtained for the extreme cases by HLN[14] and ILP[16]. To find the origin of this structure, we also plot the separate contributions from individual channels (i.e. $W_1X_{11}, W_2X_{22}, W_3X_{33}, W_1X_{44}$ - see Eq. 26). As explained in the previous section, Channel 3 yields a conventional logarithmic contribution to WAL, since this channel corresponds to the spin singlet which is unaffected by spin-orbit coupling. The other three channels give α-dependent negative contributions. We can see that the intermediate plateau structure comes from Channels 1 and 2, which have imaginary relaxation lengths in the intermediate regime. Comparing this structure with the behavior of the complex coherence lengths illustrated in Fig.4, we conclude that the crossover from the intermediate plateau to the perfect WAL plateau occurs when λ becomes real. This occurs around $\Delta_{\rm SO} \approx \eta$. For larger values of $\Delta_{\rm SO}$ the two-channel coupling $O(q^1)$ contribution is relatively less important. The evolution of this plateau region with η is illustrated in Fig.7. Here we can clearly see that the transition between the intermediate plateau and the perfect WAL plateau occurs around the line $\Delta_{\rm SO} \approx \eta$, specified by the black dashed line in the Fig.7. Note that for very weak spin-orbit coupling, WL behavior is initially enhanced. The sense of the change produced by spin-orbit coupling then changes and the crossover to WAL begins.

Quantum corrections to transport are normally studied experimentally by measuring the conductivity *vs.* temperature and external magnetic field. Both temperature and external magnetic field result mainly in modulation of the phase coherence length L. We therefore plot the L-dependence of the quantum correction ratio r in Fig.8. In this figure we see that the weak $\Delta_{\rm SO}$-dependence of r in the intermediate region commented on previously appears as a crossover from WL to WAL with increasing L that is more rapid than in the standard simplified model with phenomenological triplet channel spin-lifetimes. The L-dependence of the conductivity corrections is plotted explicitly in Fig.9 for a series of equally spaced $\Delta_{\rm SO}$ values. The intermediate and per-

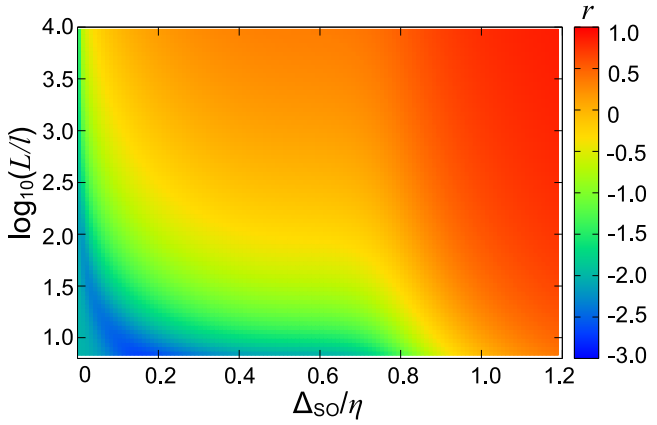

FIG. 8: (Color online) The quantum correction ratio $r(\alpha, L)$ as a function of the band splitting $\Delta_{\rm SO} = 2\alpha\bar{k}_F$ and the coherence length L. In this plot the scattering energy uncertainty is fixed at $\eta/\epsilon_F = 0.01$. All quantities are made dimensionless by setting $\epsilon_F = 2m = 1$.

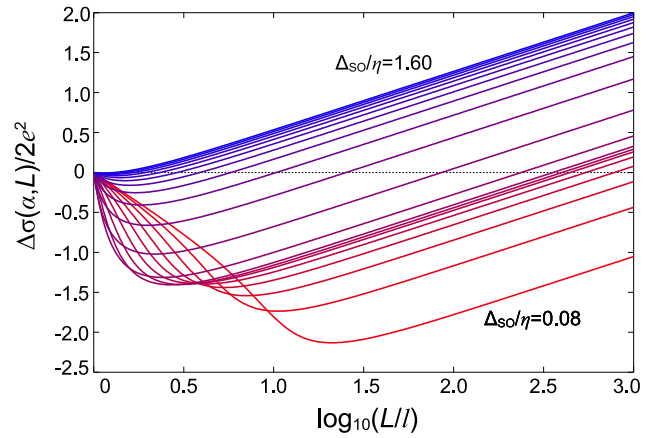

FIG. 9: (Color online) The behavior of the quantum correction amplitude $\Delta(\alpha, L)$ as a function of the coherence length L, with the spin-orbit coupling taken at $\Delta_{\rm SO}/\eta = 0.08, 0.16, 0.24, \cdots, 1.60$. The scattering amplitude is fixed at $\eta/\epsilon_F = 0.01$. All quantities are made dimensionless to setting $\epsilon_F = 2m = 1$.

fect WAL plateaus appear in this illustration as regions with densely packed lines. The slope as a function of L turns from negative (WL) to positive (WAL) around $L \sim \lambda$, and the behavior at that length scale is unconventional for intermediate spin-orbit coupling strength. However, we should note that it could be difficult to distinguish the intermediate plateau from the perfect WAL plateau by performing magneto-resistance/conductance measurements, since these measure the difference between $\Delta\sigma(L_H)$ and $\Delta\sigma(L_H = L_\epsilon)$, where the latter is the value of L in the case with no magnetic field. Such an L_H-dependence agrees with the previous magnetoconductivity calculation for an arbitrary strength of magnetic field[23]. Note however that the WAL differential behavior is conventional for $L > \lambda$, so that a relatively strong magnetic field might be necessary to observe unconventional magneto-resistance and this might give rise to other effects, such as classical magnetoresistance or Shubnikov–de Haas oscillation. Since the classical conductivity is insensitive to the spin-orbit coupling strength as long as $\Delta_{\rm SO} \ll \epsilon_F$, measurements of the α-dependence at fixed temperature and magnetic field might be able to distinguish the two plateaus and might be possible if α is tuned by varying the electric field at fixed carrier density in a two-dimensional sample with both front and back gates.

V. CONCLUSION

In this paper, we have examined the crossover behavior between WL and WAL in a two-dimensional electron gas that is triggered by variation of the Rashba spin-orbit coupling strength. We have used a numerical approach to evaluate the Cooperon contribution to the conductivity, assuming only that the energy-uncertainty of Bloch states η due to disorder scattering is small compared to the Fermi energy and treating spin-orbit coupling in a non-perturbative fashion. For this reason we are able to evaluate quantum corrections to the conductivity for any value of the ratio of the Rashba spin-splitting to disorder broadening η; an approach applicable beyond the band-unresolved limit when $\Delta_{\rm SO} \ll \eta$. When $\Delta_{\rm SO} \gg \eta$, there is no trace of the double degeneracy and each band contributes independently to the conductivity. In this limit, the system exhibits perfect WAL behavior, where the quantum interference for spin triplet combinations quickly vanishes within the order of the mean free path. In the strong spin-orbit coupling limit, the Cooperon has the same structure as that for the 2D Dirac Hamiltonian, since the band eigenstates of the two models are identical. On the other hand, when $\Delta_{\rm SO} \lesssim \eta$, a mixing between two spin triplet particle-hole channels at first order in a long-wavelength expansion is present, which has been previously identified as an important feature of spin diffusion[8]. Here we show that this coupling has profound effect on quantum corrections to conductivity. In this regime the spin relaxation length becomes imaginary when different channels are strongly coupled, suppressing the damping of quantum interference corrections to conductivity. As a result, a new plateau-like region appears near the $\Delta_{\rm SO} = \eta$ line when the maximally crossed diagrams are evaluated as a function of spin-orbit coupling strength at fixed phase coherence length. Although it seems difficult to identify these two plateaus by the investigation of the differential behavior by L, like the magneto-resistance/conductance measurement under a finite magnetic field, we suggest that they can be distinguished by tuning the spin-orbit coupling strength by an external gate voltage and fixing the coherence length (temperature and magnetic field).

Although we have limited our attention here to a simple model with spin-independent disorder scattering and

a single spin-split band that has circularly symmetric Fermi surfaces, the numerical approach we have taken is readily generalized to an arbitrary band model and to models with spin-dependent disorder scattering. Dealing with anisotropy requires only that an angular average over the Fermi surface be added to sums over band state labels. Qualitative aspects of the Rashba model results reported on here apply to other two-dimensional electron systems with broken inversion symmetry. For two-dimensional electron systems, inversion symmetry can usually be varied *in situ* by tuning gate voltages. For any two-dimensional electron system without inversion symmetry, the double spin-degeneracy of the Bloch bands is lifted by spin-orbit coupling. When the spin-splitting Δ_{SO} is larger than the Bloch state energy uncertainty η, the spin-split bands can be viewed as distinct independent bands with momentum-dependent spin-orientations. It follows that in this regime, the spin-relaxation length is on the order the mean-free path, *i.e.* spin-memory is lost at every collision. Once this occurs we do not expect to see a crossover from WAL to WL when the phase length L is decreased by increasing the magnetic field or decreasing temperature. At weaker spin-orbit coupling strengths we do expect to see WL at some temperatures and fields. However, our study shows that the way in which a WL regime emerges at weaker spin-orbit coupling can be nontrivial and is determined by specific features of the band structure of a particular system.

One potentially interesting application of our approach is to two-dimensional electron gases formed at oxide heterojunctions, for instance to the t_{2g} electron-gas systems at the interface between $LaAlO_3$ and $SrTiO_3$[24]. It is known that Rashba spin-orbit splitting in these systems[25,26] is strongest near the avoided crossing between two higher energy (lower density) elliptical xz, yz subbands and a lower energy (higher density) xy subband. The current analysis is relevant for the xy subbands away from these avoided crossings. In general, however, the Fermi surface of the electron gas at the $LaAlO_3/SrTiO_3$ interface is multi-band and multi-orbital. There are indeed indications that magnetoresistive transport anomalies occur when the Fermi level is near these weakly avoided crossings[27], suggesting that detailed analysis may reveal rich spin-relaxation physics. While it is beyond the scope of the present paper, our approach can straightforwardly be applied to the mixing of multiple orbital degrees of freedom.

Another potentially interesting system is two dimensional electron gases formed in the layers of transition metal dichalcogenide two-dimensional materials. Spin-orbit coupling and band spin-splitting is particularly strong in the valence bands of this class of materials. Coupling between spin and other degrees of freedom MoS_2[28], may give rise to interesting complex behavior[29], although we note that studies of transport in these materials are at a very early stage[30].

Acknowledgments

YA is supported by a Japan Society for the Promotion of Science Postdoctoral Fellowship for Research Abroad (No.25-56). Work at the University of Texas was supported by the Welch Foundation under grant TBF1473 and by the DOE under Division of Materials Science and Engineering grant DE-FG03-02ER45958.

Appendix A: Calculating the Cooperon and the weight factor by contour integration

In this section, we discuss in detail the procedure we use to obtain Cooperon and weight factor matrices. The key ingredient here is to split the Green's function into a sum of contributions from each band:

$$\hat{G}^{\pm}(\mathbf{k}) = \sum_n \frac{\psi_n(\mathbf{k})\psi_n^{\dagger}(\mathbf{k})}{g_n^{\pm}(\mathbf{k})}, \tag{A1}$$

where $\psi_n(\mathbf{k})$ is the eigenfunction for band $n(=\pm 1)$ in momentum and spin representation, and $g_n^{\pm}(\mathbf{k}) = \epsilon_F - E_n(\mathbf{k}) \pm i\eta$. In our 2DEG model, the Green's function simplifies to,

$$\hat{G}^{\pm}(\mathbf{k}) = \sum_n \frac{1}{2g_n^{\pm}(k)} \begin{pmatrix} 1 & -ine^{-i\phi} \\ ine^{i\phi} & 1 \end{pmatrix}. \tag{A2}$$

Since the band structure is isotropic, the denominator is independent of ϕ, the direction of the wave vector $\mathbf{k}$. Similarly, the velocity matrix $\hat{v}_\theta = \hat{v}_x \cos\theta + \hat{v}_y \sin\theta$ can be written as

$$\hat{v}_\theta(\mathbf{k}) = \sum_n \frac{v_n(k)}{2} \begin{pmatrix} \cos(\theta-\phi) & ine^{-i\theta} \\ -ine^{i\theta} & \cos(\theta-\phi) \end{pmatrix}. \tag{A3}$$

Using these expressions, the sum over $\mathbf{k}$ in Eq.(14) can be separated into integrations over the orientation ϕ and the modulus k of band wave vector. The phase integration eliminates elements which vary like $\exp(im\phi)$ for some non-zero value of m and hence determines the matrix structure. The integrations over k have the general form

$$\int_0^\infty dk\ k \frac{f_{m_1\cdots m_j}^{n_1\cdots n_j}(k)}{g_{n_1}^{+}(k)\cdots g_{n_j}^{+}(k)\ g_{m_1}^{-}(k)\cdots g_{m_j}^{-}(k)}. \tag{A4}$$

They can be completed by extending the path of integration into a large contour in the complex plane and using Cauchy's theorem. If we choose to close the contour in the upper half complex plane, the poles $\bar{k}_n$ are given by the solutions of the equations $g_n^{+}(\bar{k}_n) = 0$. As long as we limit the disorder strength to lie within the diffusive regime $\eta \ll \epsilon_F$, we can solve this equation by using a gradient expansion around the Fermi surface,

$$g_n^{+}(\bar{k}_n) \simeq v_F(\bar{k}_n - k_{Fn}) + i\eta. \tag{A5}$$

By summing over the band indices, we determine the values of the matrix elements. Because the resulting expressions are extremely cumbersome, we have evaluated the residues and summed over band indices numerically. In the following subsections, we show how the matrix elements can be constructed at each order in q-expansion.

1. $O(q^0)$

To leading order in the q-expansion, we obtain the form

$$\check{P}^{(0)} = p_1^{(0)} \begin{pmatrix} 1 & & & \\ & 1 & & \\ & & 1 & \\ & & & 1 \end{pmatrix} - p_2^{(0)} \begin{pmatrix} & & & 0 \\ & & 1 & \\ & 1 & & \\ 0 & & & \end{pmatrix} \tag{A6}$$

in the tensor product basis, where

$$p_1^{(0)} = \sum_{n,m} I_{n,m}^{(0)}, \quad p_2^{(0)} = \sum_{n,m} I_{n,m}^{(0)} nm, \tag{A7}$$

$$I_{n,m}^{(0)} = \frac{1}{2\pi} \int dk \frac{k}{4 g_n^+ g_m^-}. \tag{A8}$$

The coefficients in the singlet-triplet basis are

$$A_1^{(0)} = A_4^{(0)} = \gamma^{-1} - p_1^{(0)}, \; A_2^{(0)} = \gamma^{-1} - p_1^{(0)} + p_2^{(0)}. \tag{A9}$$

We can show analytically that $A_3^{(0)} = \gamma^{-1} - p_1^{(0)} - p_2^{(0)}$ vanishes at any value of α: Since $p_1^{(0)} + p_2^{(0)} = \sum_{n,m}(1 + nm) I_{n,m}^{(0)}$ vanishes when $nm = -1$, only particle-hole pairs with band indices $n = m$ contribute to $A_3^{(0)}$. Taking the residual value, we obtain

$$I_{n,n}^{(0)} = \frac{i\bar{k}_n}{-4 v_F g_n^-(\bar{k}_n)} \sim \frac{k_{Fn}}{8 v_F \eta} = \frac{1}{4\gamma}, \tag{A10}$$

where we have used $g_n^-(\bar{k}_n) = g_n^+(\bar{k}_n) - 2i\eta = -2i\eta$. Therefore, $p_1^{(0)} + p_2^{(0)} = \gamma^{-1}$, which leads to $A_3^{(0)} = 0$.

2. $O(q^1)$

At linear and the quadratic orders in the q-expansion, we should note that $\hat{G}^{\pm} \hat{v}_\theta \hat{G}^{\pm}$ in Eq.(14) can be decomposed as

$$\begin{aligned} (\hat{G}^{\pm} \hat{v}_\theta \hat{G}^{\pm})(\mathbf{k}) = & \sum_{n_1 n_2 n_3} \frac{v_{n_2}}{8 g_{n_1}^{\pm} g_{n_3}^{\pm}} \left(n_2 - \frac{n_1 + n_3}{2} \right) \\ & \times \left[\begin{pmatrix} 0 & ie^{-i\theta} \\ -ie^{i\theta} & 0 \end{pmatrix} - (n_1 + n_3) \cos(\theta - \phi) \begin{pmatrix} 1 & 0 \\ 0 & 1 \end{pmatrix} \right. \\ & \left. + n_1 n_3 \begin{pmatrix} 0 & ie^{i(\theta - 2\phi)} \\ -ie^{i(2\phi - \theta)} & 0 \end{pmatrix} \right]. \end{aligned} \tag{A11}$$

Substituting this decomposition to Eq.(14) and integrating out the phase ϕ, we obtain the matrix decomposition of $\check{P}_\theta^{(1)}$ in the tensor product basis,

$$\begin{aligned} \check{P}_\theta^{(1)} = & \\ & p^{(1)} \begin{pmatrix} & & \Theta^* & \\ & & & \Theta^* \\ \Theta & & & \\ & \Theta & & \end{pmatrix} - (p^{(1)})^* \begin{pmatrix} & -\Theta^* & & \\ -\Theta & & & \\ & & & \Theta \\ & & \Theta^* & \end{pmatrix}, \end{aligned} \tag{A12}$$

with the shorthand notation $\Theta = -ie^{i\theta}$. Here the factor $p^{(1)}$ is defined by

$$p^{(1)} = \frac{1}{2} \sum_{n m_1 m_2 m_3} \left[\left(I_{n m_1 m_2 m_3}^{(1)} \right)^* - n m_1 I_{n m_1 m_2 m_3}^{(1)} \right], \tag{A13}$$

$$I_{n m_1 m_2 m_3}^{(1)} = \frac{1}{2\pi} \int dk \frac{k v_{m_2}}{16 g_n^+ g_{m_1}^- g_{m_3}^-} \left(m_2 - \frac{m_1 + m_3}{2} \right). \tag{A14}$$

Applying the unitary transformation by $\check{T}_\theta$, we obtain the correspondence to the coefficients in the singlet-triplet basis,

$$A_{12}^{(1)} = \mathrm{Re}\; p^{(1)}, \quad A_{34}^{(1)} = -\mathrm{Im}\; p^{(1)}. \tag{A15}$$

It should be noted that the linear term in q is not diagonal even in the singlet-triplet basis, and accounts for the coupling between different channels at finite momentum.

3. $O(q^2)$

Substituting the decomposition in Eq.(A11) to Eq.(14), we obtain the matrix decomposition of $\check{P}_\theta^{(2)}$ in the tensor product basis,

$$\begin{aligned} \check{P}_\theta^{(2)} = & -p_1^{(2)} \begin{pmatrix} & & & -e^{-2i\theta} \\ & & 1 & \\ & 1 & & \\ -e^{2i\theta} & & & \end{pmatrix} + p_2^{(2)} \begin{pmatrix} 1 & & & \\ & 1 & & \\ & & 1 & \\ & & & 1 \end{pmatrix} \\ & - p_3^{(2)} \begin{pmatrix} & & & 0 \\ & & 1 & \\ & 1 & & \\ 0 & & & \end{pmatrix}, \end{aligned} \tag{A16}$$

with the coefficients

$$p_1^{(2)} = \sum_{\{n,m\}} I_{\{n,m\}}^{(2)}, \quad p_2^{(2)} = \sum_{\{n,m\}} 2 n_1 m_1 I_{\{n,m\}}^{(2)}, \tag{A17}$$

$$p_3^{(2)} = \sum_{\{n,m\}} n_1 n_3 m_1 m_3 I_{\{n,m\}}^{(2)},$$

$$I_{\{n,m\}}^{(2)} = \int \frac{dk}{2\pi} \frac{k v_{n_2} v_{m_2} (2n_2 - n_1 - n_3)(2m_2 - m_1 - m_3)}{512 g_{n_1}^+ g_{n_3}^+ g_{m_1}^- g_{m_3}^-}, \tag{A18}$$

where $\{n,m\}=\{n_1,n_2,n_3,m_1,m_2,m_3\}$. This can be diagonalized by the unitary transformation $\check{T}_\theta$, which leads to the following connection to the singlet-triplet basis:

$$A_1^{(2)}=-p_1^{(2)}+p_2^{(2)},\quad A_2^{(2)}=-p_1^{(2)}+p_2^{(2)}-p_3^{(2)},\quad A_4^{(2)}=p_1^{(2)}+p_2^{(2)},\quad A_3^{(2)}=p_1^{(2)}+p_2^{(2)}-p_3^{(2)}. \tag{A19}$$

4. Weight factor

The decomposition in Eq.(A11) can also be applied to the calculation of the weight factor matrix. Substituting the decomposition to the definition of weight factor matrix in Eq.(9) and integrating out the phase ϕ, we obtain the form in Eq.(25), with

$$R_1=\sum_{\{n,m\}}J_{\{n,m\}},\quad R_2=\sum_{\{n,m\}}(n_1m_3+n_3m_1)J_{\{n,m\}}, \tag{A20}$$

$$R_2'=\sum_{\{n,m\}}(n_1m_1+n_3m_3)J_{\{n,m\}},$$

$$R_3=\sum_{\{n,m\}}n_1n_3m_1m_3J_{\{n,m\}},$$

$$J_{\{n,m\}}=\int\frac{dk}{2\pi}\frac{kv_{n_2}v_{m_2}}{64g_{m_1}^+g_{n_3}^+g_{n_1}^-g_{m_3}^-}\left(n_2-\tfrac{n_1+n_3}{2}\right)\left(m_2-\tfrac{m_1+m_3}{2}\right).$$

The definition of $J_{\{n,m\}}$ looks similar to $I^{(2)}_{\{n,m\}}$, while the difference appears in the retarded/advanced indices in the denominator. We should note that (n_1,n_3) and (m_1,m_3) cannot be exchanged here, respectively.

[1] Yu. A. Bychkov and E. I. Rashba, J. Phys. C **17**, 6093 (1984).
[2] J. Nitta, T. Akazaki, H. Takayanagi, and T. Enoki, Phys. Rev. Lett. **78**, 1335 (1997); T. Koga, J. Nitta, H. Takayanagi, and S. Datta, Phys. Rev. Lett. **88**, 126601 (2002).
[3] S. Datta and B. Das, Appl. Phys. Lett. **56**, 665 (1990).
[4] J. Alicea, Rep. Prog. Phys. **75**, 076501 (2012).
[5] R. J. Elliott, Phys. Rev. **96**, 266 (1954).
[6] Y. Yafet, Solid State Phys. **14**, 1 (1963).
[7] M. I. D'yakonov and V. I. Perel', Sov. Phys. Solid State **13**, 3023 (1972).
[8] A. A. Burkov, A. S. Núñez, and A. H. MacDonald, Phys. Rev. B **70**, 155308 (2004).
[9] E. G. Mishchenko, A. V. Shytov, and B. I. Halperin, Phys. Rev. Lett. **93**, 226602 (2004).
[10] E. Abrahams, P. W. Anderson, D. C. Licciardello, and T. V. Ramakrishnan, Phys. Rev. Lett. **42**, 673 (1979).
[11] L. G. Gorkov, A. I. Larkin, and D. E. Khmel'nitzkii, JETP Lett. **30**, 228 (1979); B. L. Altshuler, D. Khmel'nitzkii, A. I. Larkin, and P. A. Lee, Phys. Rev. B **22**, 5142 (1980).
[12] G. Bergmann, Phys. Rep. **107**, 1 (1984).
[13] E. Akkermans and G. Montambaux, *Mesoscopic Physics of Electrons and Photons*, (Cambridge University Press,2007).
[14] S. Hikami, A. I. Larkin, and Y. Nagaoka, Prog. Theor. Phys. **63**, 707 (1980).
[15] S. Hikami, Phys. Rev. B **24**, 2671 (1981).
[16] S. V. Iordanskii, Yu. B. Lyanda-Geller, and G. E. Pikus, JETP Lett. **60**, 206 (1994); W. Knap *et al.*, Phys. Rev. B **53**, 3912 (1996).
[17] T. Koga, J. Nitta, T. Akazaki, and H. Takayanagi, Phys. Rev. Lett. **89**, 046801 (2002).
[18] E. B. Olshanetsky *et al.*, JETP Lett. **91**, 347 (2010).
[19] J. Chen *et al.*, Phys. Rev. Lett. **105**, 176602 (2010).
[20] H.-T. He *et al.*, Phys. Rev. Lett. **106**, 166805 (2011).
[21] J. G. Checkelsky, Y. S. Hor, R. J. Cava, and N. P. Ong, Phys. Rev. Lett. **106**, 196801 (2011).
[22] A. D. Caviglia *et al.*, Phys. Rev. Lett. **104**, 126803 (2010).
[23] L. E. Golub, Phys. Rev. B **71**, 235310 (2005); M. M. Glazov and L. E. Golub, Semicond. Sci. Technol. **24**, 064007 (2009).
[24] J. A. Sulpizio, S. Ilani, P. Irvin, and J. Levy, Annual Review of Materials Research **44**, (2014); S. Stemmer and S. J. Allen, Annual Review of Materials Research **44**, (2014); H. Y. Hwang, Y. Iwasa, M. Kawasaki, B. Keimer, N. Nagaosa, and Y. Tokura, Nature Materials **11**, (2012).
[25] G. Khalsa, B. Lee, and A. H. MacDonald, Phys. Rev. B **88**, 041302 (2013).
[26] Z. Zhong, A. Tóth, and K. Held, Phys. Rev. B **87**, 161102 (2013).
[27] A. Joshua, S. Pecker, J. Ruhman, E. Altman, and S. Ilani, Nat. Commun. **3**, 1129 (2012).
[28] D. Xiao, G.-B. Liu, W. Feng, X. Xu, and Wa. Yao, Phys. Rev. Lett. **108**, 196802 (2012).
[29] H.-Z. Lu, W. Yao, D. Xiao, and S.-Q. Shen, Phys. Rev. Lett. **110**, 016806 (2013).
[30] A. T. Neal, H. Liu, J. Gu , and P. D.Ye, ACS Nano **7**, 7077 (2013).